Post-Print

This is the accepted version of:

Poly-dispersed Eulerian-Lagrangian particle tracking for in-flight icing applications

Giuseppe A. G. Sirianni* and Tommaso Bellosta† and Barbara Re‡ and Alberto Guardone§
Politecnico di Milano, Milan, 20156, Italy

The objective of this work is to present a three-dimensional Euler-Euler finite volume poly-dispersed (multi-bin) droplet tracker for in-flight icing purposes, with an additional Lagrangian re-injection step. This step has been added to increase the accuracy of the collection efficiency prediction in multi-element 2D and 3D cases where splashed and rebounding droplets re-impinge on aft surfaces, particularly in SLD conditions. Results show local increases in accuracy of up to 4% in a 3D single element case and up to 100% on flaps in 2D multi-element airfoil cases. The Lagrangian re-impingement correction improves significantly when using multi-bin, while also being more efficient than the standard approaches. Lastly, a simple bin to bin initialization strategy allows for up to 65% less computational time in the Eulerian droplet tracking step when running multi-bin simulations.

Nomenclature

α	=	water volume fraction $[-]$
β	=	collection efficiency $[-]$
μ	=	dynamic viscosity $[Pa/s]$
σ	=	surface tension $[N/m]$
π	=	relaxation pseudo pressure $[m^2/s^2]$
ρ	=	density $[kg/m^3]$
θ	=	impingement angle (from plane tangent toward droplet velocity) $[deg]$
$area$	=	surface mesh element area $[m^2]$
c	=	relaxation constant $[m/s]$
d_P	=	droplet diameter $[m]$
K	=	Mundo splashing parameter
K_L	=	LEWICE splashing parameter
$K_{L,n}$	=	LEWICE normal splashing parameter
$\dot{n}$	=	normal number flux of droplets $[1/s]$
S_{disc}	=	LEWICE splashing discriminator
Oh	=	Ohnesorge number $[-]$
$\dot{m}$	=	mass flux caught by surface element in Lagrangian re-impingement $[kg/s]$
MVD	=	mean volumetric diameter $[m]$
LWC	=	liquid water content $[kg/m^3]$
$\dot{LWC}$	=	liquid water content surface normal flux $[kg/m^2 s]$
$\underline{U}$	=	air velocity $[m/s]$
$\underline{u}_P$	=	droplet velocity $[m/s]$
$\underline{f}_D$	=	drag force $[N]$
$\hat{n}$	=	unit surface normal vector $[-]$
$\hat{t}$	=	unit surface tangential vector $[-]$
$(\cdot)_P$	=	droplet related quantity
$(\cdot)_f$	=	air-flow or fluid related quantity

---

*Aerospace Engineer, Dipartimento di Scienze e Tecnologie Aerospaziali DAER
†Ph.D Student, Dipartimento di Scienze e Tecnologie Aerospaziali DAER
‡Assistant Professor, Dipartimento di Scienze e Tecnologie Aerospaziali DAER
§Full Professor, Dipartimento di Scienze e Tecnologie Aerospaziali DAER

$(\cdot)_i$	=	incoming (pre-splashing) quantity
$(\cdot)_s$	=	splashed (post-splashing) quantity
$(\cdot)^j$	=	*j-th* bin quantity
$(\cdot)^{L,R}$	=	left/right quantity in the Riemann problem

I. Introduction

IN-FLIGHT icing is a major threat to air-borne vehicles as ice accreting on aerodynamic surfaces can deteriorate aerodynamic performance, and it may induce safety concerns. Indeed, if a chunk of ice detaches, for instance because of the deployment of an ice protection system or because of aerodynamic forces, it can cause considerable damage to aft components such as the first stages of a compressor or the tail empennage [1]. Numerical simulation of the in-flight ice accretion process is a complex task and requires to consider different aspects. One of them is the computation of the trajectories of the water droplets impinging on aerodynamic surfaces. This information is then used to obtain the amount of water being caught, measured using the collection efficiency β.

The computation of the droplet impingement requires to solve a two-phase problem, characterized by an arbitrarily large number of droplets of water embedded in the air flow. In principle, the dynamic interaction and the transfer processes among phases could, be taken into account by using an Eulerian two-fluid model. Such a model consists in two sets of augmented conservation laws, one per each phase, which include suitable transport terms to account for the interaction between phases. The most general models, such as the Baer-Nunziato model and its variants, e.g., [2, 3], allow each phase to evolve with its own density, pressure, and temperature, whereas reduced two-fluid models assume equilibrium in certain variables [4]. However, since ice accretion simulations typically involve dispersed flows, where one phase, i.e., water, is dilute and composed of small particles dispersed inside the carrier phase, i.e., air, the effect of the droplets on the air flow field can be neglected and the assumption of a one-way coupling is generally introduced [5]. In this way, the water-air problem is decoupled: first, the air flow field is solved, neglecting the preference of the water droplets, then the motion of water droplet is computed. This latter task can be approached in two ways: by tracking each interface individually, following a Lagrangian approach, which however is not practical when a large number of droplets is involved, or following the Eulerian approach, which describes the droplets as a continuous phase and expresses the amount of water in a unitary control volume through the concept of volume fraction α.

Currently, most of the research effort in the field of in-flight icing simulation is aimed at obtaining a better understanding of the behavior of Appendix O, which describes potential conditions for the so-called supercooled large droplet (SLD) icing, characterized by water droplets with a median volumetric diameter (*MVD*) larger than 40 μm. In SLD icing, large droplets may bounce or splash, depending on the angle they hit the surface with. Hence, part of the droplet mass is not deposited at the impingement location, but it re-enters the flow-field, potentially resulting in re-impingement [6, 7]. For this reason, a new Lagrangian re-injection step has been developed in this work to track these secondary droplets and compute an additional collection efficiency. Thanks to this step, it is possible to increase the agreement with experimental data, while also not increasing the computational cost excessively.

The Lagrangian approach has been followed for the re-injection instead of an Eulerian approach for two main reasons. First, the re-injection in the Eulerian approach would require a decoupling of the pre- and postimpact droplet boundary conditions, that is each airfoil surface mesh element should be converted one by one from an outlet of droplets to an inlet of re-injected droplets, which is extremely costly [8]. Second, the heterogeneous nature of the re-injected droplets is well suited for individual tracking (Lagrangian) rather than for a two fluid approach (Eulerian). This heterogeneousness is further increased by considering poly-dispersity by using a multi-bin approach, therefore subdividing the free-stream cloud into a finite number of so called bins, characterized by their droplet diameter and liquid water content. The solution of each of these bins is computed separately, and then combined for the final results.

Before tracking the secondary droplets, the free-stream cloud must be simulated. For this an Euler-Euler approach is used to track droplets over two and three dimensional unstructured meshes in order to compute the collection efficiency due to the free-stream cloud. In an Eulerian frame of reference, the particle tracking equations are written as the pressureless gas dynamics system plus a source term coupling the particles to the fluid flow. In this work, the hyperbolic part of the system was relaxed in order to recover strict hyperbolicity, following Berthon et al. [9]. The resulting equations are solved using a second order finite volume solver. The collection efficiency is then corrected to account for mass loss due to droplet splashing and rebounding using the model presented by Wright [10]. The removed mass is then re-injected using the Euler-Lagrange approach in order to compute the re-impingement collection efficiency.

Re-impingement of secondary droplets has been shown to be important by Rutkowski et al. [11], with splashed droplets possibly re-impinging far from their original impact location. Papadakis et al. [12] showed that considering

splash-back does indeed improve collection efficiency results, same as Fouladi et al. [13] who also highlighted the increased importance in Appendix O conditions. Bilodeau and Habashi [8] studied a fully Eulerian re-injection procedure, finding it to be useful in increasing the agreement with experimental data in SLD conditions, but with an extreme computational cost increase (ranging from 500% up to 900%) even when limiting the computational grid. For these reasons, this work on the development of an Eulerian droplet tracker with Lagrangian re-injection has allowed to reap the benefits of re-injection on the collection efficiency prediction while not costing too much in terms of computational time.

The multi-bin Eulerian solver with Lagrangian re-injection developed in this work has been tested against experiments from Papadakis et al. [6, 14], namely a 2D NACA 23012, a 2D three-element airfoil and a 3D horizontal swept tail in a wind tunnel. A simple bin restart strategy has been used to mitigate the inherent computational cost increase of the Eulerian multi-bin simulation and its effects have been evaluated, together with the added cost of the Lagrangian re-injection step.

The paper is structured as follows: the numerical tools used and developed in this work are presented in section II. To do this, in section II.A the Eulerian droplet tracking tool developed for this work in SU2 [15] is summarized. After this, the Lagrangian re-injection step is described in section II.B. Then the Eulerian multi-bin solver is validated, and the Lagrangian re-injection mass conservativity is assessed in section III.A. Finally, results for the complete mixed Eulerian-Lagrangian solver are presented in section III.B, together with a note on the computational costs of both the multi-bin Eulerian simulation and the Lagrangian re-injection.

II. Method

All droplet tracking simulations for in-flight icing applications are performed with a main objective in mind: computing the collection efficiency β on the aircraft's surface. The collection efficiency (depicted graphically in Fig. 1) is a measure of the fraction of water being captured by a point on the surface with respect to the water present in the free-stream cloud.
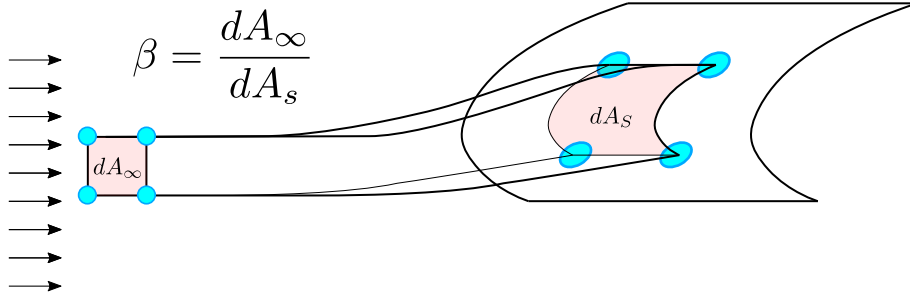
Fig. 1   Collection efficiency geometrical definition. In red, the cross-sectional areas of the droplet stream tube at the far-field, dA_∞, and on the wing surface dA_S.

A. Eulerian Droplet Tracking

To compute the Euler-Euler droplet trajectories, the carrier fluid field is obtained by solving the Euler equations, whereas the particles equations are computed from the solution of the relaxed pressureless gas dynamics (PGD) system of Berthon et al. [9] (Eq. (1)).

$$\begin{cases} \frac{\partial \alpha}{\partial t} & + \overline{\nabla} \cdot \left(\alpha \underline{u}_p \right) = 0 \\ \frac{\partial \alpha \underline{u}_p}{\partial t} & + \overline{\nabla} \cdot \left(\alpha \underline{u}_p \otimes \underline{u}_p + \pi \underline{\underline{I}} \right) = \alpha \underline{f}_D \left(\underline{U} - \underline{u}_p, C_D \left(Re_d \right), Re_d, droplet\, fluid, air\, fluid \right) \\ \frac{\partial \alpha \pi}{\partial t} & + \overline{\nabla} \cdot \left(\alpha \pi \underline{u}_p + c^2 \underline{u}_p \right) = -\lambda \alpha \pi \end{cases} \quad (1)$$

where the term $\alpha \underline{f}_D$ in Eq. (1) is modelling the momentum transfer between the carrier phase (air) and the dispersed phase (droplets) due to the drag generated by the slip velocity $\underline{U} - \underline{u}_p$. More on the drag model will follow. The third equation, is an equation for the pseudo-pressure relaxation. This equation will not be solved explicitly due to the assumption of pseudo-pressure equilibrium ($\pi = 0$ in the control volumes) but its effects will appear in the

Riemann problem solution. This will decrease both memory requirements and computational costs while maintaining the numerical benefits.

Both sets of equations (fluid and particles) are discretized using the finite volume method with a standard edge-based structure on a dual grid with control volumes constructed using a median-dual vertex-based scheme in SU2 [15]. Convective fluxes are discretized using a limited second-order MUSCL scheme with the Venkatakrishnan slope limiter. For the Euler equations, the approximate Riemann solver of Roe is employed, whereas for the particle tracking system the exact Riemann problem is solved at each edge to compute the fluxes. Source terms are approximated at each node using a piecewise-constant reconstruction within each control volume. Gradients are obtained via a weighted least-squares approach. A time-marching approach is used to drive the systems to the steady state using an implicit Euler scheme. The exact solution of the exact 1D Riemann problem is reported in Eq. (2) assuming pseudo-pressure equilibrium in the control volumes ($\pi = 0$). The reader is referred to Berthon et al. [9] for a more in depth description.

	Left State	Left* State	Right* State	Right State
$\alpha =$	α^L	$\dfrac{2\alpha^L c}{2c - \alpha^L \left(u_p^L - u_p^R\right)}$	$\dfrac{2\alpha^R c}{2c - \alpha^R \left(u_p^L - u_p^R\right)}$	α^R
$u_p =$	u_p^L	$\dfrac{u_p^L + u_p^R}{2}$	$\dfrac{u_p^L + u_p^R}{2}$	u_p^R
$\pi =$	0	$c\dfrac{u_p^L - u_p^R}{2}$	$c\dfrac{u_p^L - u_p^R}{2}$	0

$$(2)$$

It is important to note that Eq. (2) is a valid solution to the 1D Riemann problem under the assumption that the relaxation constant c satisfies $c > \max\left(0, \ \alpha^L \frac{u^L - u^R}{2}, \ \alpha^R \frac{u^L - u^R}{2}\right)$. In addition, in order for the scheme to be able to approximate vacuum solutions without the time step going to zero, Berthon et al. [9] state that, for $\varepsilon > 0$ and $c > \max\left(0, u_P^R - u_P^L\right)$, one can take:

$$
c = \begin{cases} \max\left[0, \max\left(\alpha^i, \alpha^j\right)\left(u_p^i - u_p^j\right)\right] & \text{if } u_p^i \geq u_p^j \\ \min\left[\varepsilon, \frac{1}{2}\min\left(\alpha^i, \alpha^j\right)\left(C + u_p^i - u_p^j\right)\right] & \text{if } u_p^i < u_p^j \end{cases}
$$

$$(3)$$

In the PGD system given by Eqs. (1), the only source of (one way) coupling between flow and particles is the drag momentum source term $\alpha \underline{f}_D$.

$$
\alpha \underline{f}_D = \alpha \frac{C_D Re_d}{24K}\left(\underline{U} - \underline{u}_p\right) \qquad \text{where} \qquad K = \frac{\rho_p d_p^2 U_\infty}{18\mu_f} \qquad \text{and} \qquad Re_d = \frac{\rho_f \left|\underline{U} - \underline{u}_p\right| d_p}{\mu_f}
$$

$$(4)$$

The drag coefficient C_D is modeled by initially assuming the droplet to be a sphere, using the approximation by Morrison [16] and Clift et. al. [17], according to the Reynolds number computed on the basis of the slip velocity between air and droplets, as

$$
C_D^{\text{sphere}}(Re_d) = \begin{cases} C_{D,\text{Morrison}}^{\text{sphere}} & Re_d < 10^6 \\ C_{D,\text{Clift et. al.}}^{\text{sphere}} & Re_d > 10^6 \end{cases}
$$

$$(5)$$

In the SLD regime, due to the large diameter, the particles undergo significant deformation. The effects of deformation are modeled through a simple semi-empirical model that provides a modified drag coefficient [17]. To be able to account for the eccentricity brought in by the deformation in the SLD regime, the Weber breakup number from Honsek et al. [18] is introduced in Eq. (6).

$$
We_b = d_p \left|\underline{u}_p\right|^2 \frac{\rho_f}{\sigma_p}
$$

$$(6)$$

This is then used to compute the eccentricity f as in Honsek et al. [18]

$$
f = \left[\frac{1}{1 + 0.07\sqrt{We_b}}\right]^6
$$

$$(7)$$

4

The eccentricity is finally used to linearly interpolate the C_D between the sphere's drag coefficient C_D^{sphere} and the disk's drag coefficient C_D^{disk} as in Eq. (8).

$$C_D\left(Re_d\right) = \begin{cases} (1-f)C_D^{\text{sphere}} + fC_D^{\text{disk}} & We_b \leq 12 \\ C_D^{\text{disk}} & We_b > 12 \end{cases} \tag{8}$$

where the disk's drag coefficient C_D^{disk} is taken from Clift et. al. [17] and defined as in Eq. (9). After $We_b > 12$ the droplet should breakup, but in this work this phenomena is not considered, hence the assumption of $C_D = C_D^{\text{disk}}$ beyond $We_b > 12$.

$$C_D^{\text{disk}}\left(Re_d\right) = \begin{cases} \dfrac{64}{\pi Re_d}\left(1 + \dfrac{Re_d}{2\pi}\right) & Re_d \leq 0.01 \\[3mm] \dfrac{64}{\pi Re_d}\left(1 + 10^{-0.883 + 0.906\log_{10}(Re_d) - 0.025\left(\log_{10}(Re)\right)^2}\right) & Re_d \in (0.01, 1.5] \\[3mm] \dfrac{64}{2\pi}\left(1 + 0.138 Re_d^{0.792}\right) & Re_d \in (1.5, 133] \\[3mm] 1.17 & Re_d > 133 \end{cases} \tag{9}$$

Polydispersity of droplets inside a cloud is taken into account by performing multi-bin simulations. Indeed, *MVD* represents an average diameter of the free-stream cloud and can provide adequate impingement predictions, but the dispersed droplets actually exhibit a wide range of diameters. For this reason, the droplets in a cloud are sampled in a discrete number of sets (called bins), each one characterized by a specific liquid water content percentage LWC^i [%] and droplet diameter d_p^i. Each bin is then simulated independently, and the results are combined to obtain the total collection efficiency of a multi-bin Eulerian simulation at a certain position $\underline{x}$ on the surface as Eq. (10). This collection efficiency is the one due to the free-stream cloud, still not corrected to account for the mass lost due to splashing and bouncing.

$$\beta_i(\underline{x}) = \sum_{j=1}^{N_{bins}} \frac{LWC^j(\underline{x})\left[\underline{u}_p^j(\underline{x}) \cdot \hat{\boldsymbol{n}}(\underline{x})\right]}{LWC_\infty U_\infty} = \sum_{j=1}^{N_{bins}} LWC^j\,[\%]\left[\alpha^j(\underline{x})\frac{\underline{u}_p^j(\underline{x}) \cdot \hat{\boldsymbol{n}}(\underline{x})}{U_\infty}\right] \tag{10}$$

Since each bin is simulated independently, it is easy to see how the computational cost of a multi-bin Eulerian droplet tracking simulation becomes linear with the number of bins considered. To mitigate this, a simple bin restart procedure (recapped in Fig. 2) has been employed: each bin from $i = 2, 3, ..., N_{bins}$ is initialized using the converged solution of the previous bin for the solver to start iterating on. This means that, as long as the bins are sorted with monotone d_p^i (ascending or descending), the number of iterations needed to reach convergence will be less than starting from the classical homogeneous guess, given the higher quality initial guess.
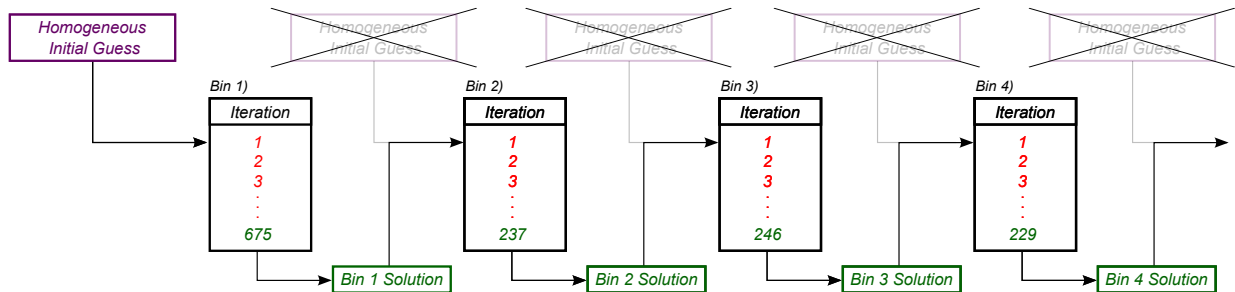
Fig. 2 Eulerian bin restart procedure: schematic example with 4 bins. Assuming the bins ordered according to their characteristic diameter, the mono-dispersed solution of bin 1 is used as initial guess for the mono-dispersed solution of bin 2, which is used for bin 3, and so on. The number of iterations needed to solve Eqs. (1) for the subsequent bins is much lower than the one required by bin 1, which is initialized with a homogeneous guess.

B. Splashing and Lagrangian Re-injection

The Lagrangian re-injection introduced in this work consists in two main steps: first, the collection efficiency is corrected to account for the mass loss due to splashing and bouncing. Second, this mass is re-injected using PoliDrop, Politecnico di Milano's in-house Lagrangian droplet tracker, in order to track the so called *secondary droplets* and compute a second collection efficiency to be added to the first one. For an in-depth description of PoliDrop the reader is referred to Bellosta et al. [19]. The momentum conservation Eq. (11) for each droplet is solved to obtain the velocity, which is then used to compute the trajectories.

$$m_p \frac{d\underline{u}_p}{dt} = \frac{\pi}{8}\mu_f d_p Re_d \left(\underline{U} - \underline{u}_p\right) C_D + \frac{\pi}{6}d_p^3 \underline{g} \left(\rho_p - \rho_f\right) \tag{11}$$

In this work, we use the splashing and bouncing model by Wright et al. [10]. To determine whether splashing occurs at a certain position $\underline{x}$ on the surface, we first need to compute the following parameters:

$$Oh = \frac{\mu_p}{\sqrt{\rho_p \sigma_p d_p}} \qquad Re_p(\underline{x}) = \frac{\rho_p \left|\underline{u}_p(\underline{x})\right| d_p}{\mu_p}$$

$$K(\underline{x}) = Oh \cdot Re_p^{\frac{5}{4}}(\underline{x}) \qquad K_L(\underline{x}) = K^{0.859}(\underline{x}) \left(\frac{\rho_p}{LWC(\underline{x})}\right)^{0.125} \tag{12}$$

$$K_{L,n}(\underline{x}) = \frac{K_L(\underline{x})}{\left[\sin\left(\theta_i(\underline{x})\right)\right]^{1.25}} \qquad S_{\text{disc}}(\underline{x}) = K_{L,n}(\underline{x}) - 200$$

Then, using the splashing discriminator S_{disc}, we can establish whether splashing occurs at that location, as shown by Eq. (13)), where the dependence on the position $\underline{x}$ has been dropped for brevity.

$$\begin{aligned} &\text{if } S_{\text{disc}} > 0 \qquad \text{splashing occurs} \\ &\text{if } S_{\text{disc}} \leq 0 \qquad \text{splashing does not occur} \end{aligned} \tag{13}$$

Given the steady nature of the Eulerian simulations, all splashing variables are expressed as fluxes of mass per unit time on a surface element in Eq. (14).

$$d_{p,s} = d_{p,i} \cdot 8.72 e^{0.0281K} \quad \left(0.05 \leq \frac{d_{p,s}}{d_{p,i}} \leq 1\right) \qquad LWC_s = LWC_i \cdot 0.7 \left(1 - \sin\theta_i\right)\left[1 - e^{-0.0092026 \cdot S_{\text{disc}}}\right]$$

$$L\dot{W}C = LWC \left(\underline{u}_p \cdot \hat{\boldsymbol{n}}\right) \qquad \dot{n}_s = \frac{mass\ flux_{splashed\ water\ on\ face}}{mass_{single\ splashed\ droplet}} = \frac{L\dot{W}C_s}{\rho_p}\frac{3\pi}{4}\left(\frac{2}{d_{p,s}}\right)^3 \cdot area$$

$$\left[\underline{u}_{p,s} \cdot \hat{\boldsymbol{n}}\right] = \left[\underline{u}_{p,i} \cdot \hat{\boldsymbol{n}}\right](0.3 - 0.002\theta_i) \qquad \left[\underline{u}_{p,s} \cdot \hat{\boldsymbol{t}}\right] = \left[\underline{u}_{p,i} \cdot \hat{\boldsymbol{t}}\right](1.075 - 0.0025\theta_i) \tag{14}$$

$$\beta_s = \beta_i \left(1 - \frac{LWC_s |\underline{u}_{p,s}|}{LWC_i |\underline{u}_{p,i}|}\right)$$

In order to guarantee that the re-injected droplets are indeed inside the computational domain, when initializing their position to start the Lagrangian re-injection simulation, these are not placed exactly at the coordinates of the node at the wall, but they are slightly displaced from the boundary, as shown in Fig. 3a. Furthermore, if needed, it is possible to split a parcel into more sub-parcels, spaced along the surface tangent as depicted in Fig. 3b, to increase the number of parcels in the domain in order to ensure there are enough of them to obtain a smooth Lagrangian collection efficiency.
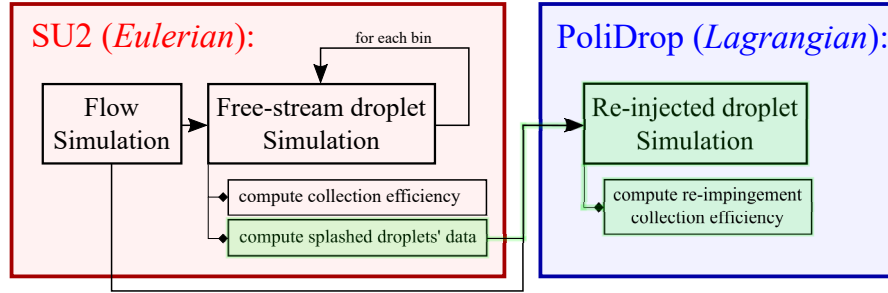
The computational scheme of the complete mixed Eulerian-Lagrangian solver is therefore recapped in Fig. 4.

The total collection efficiency at a certain point $\underline{x}$ on the surface is computed as in Eq. (15), therefore as the sum of the Eulerian collection efficiency of every bin (corrected for splashing and bouncing mass loss) weighted by the bin's *liquid water content* percentage plus the additional Lagrangian re-injection collection efficiency.

$$\beta(\underline{x}) = \sum_{j=1}^{N_{bins}} LWC^j \, [\%] \cdot \beta_s^j(\underline{x}) + \frac{\dot{m}(\underline{x})}{area(\underline{x}) \cdot LWC_\infty U_\infty} \tag{15}$$

(a)   (b)
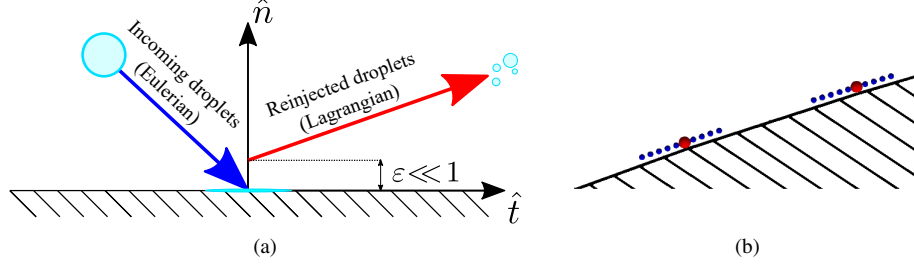
Fig. 3 Lagrangian re-injection artificial wall displacement and spacing. In Fig. 3a, the artificial displacement used to ensure droplets are inside the computational domain. In Fig. 3b, the parcel splitting technique used to increase the number of droplets being re-injected to help obtain a smoother Lagrangian collection efficiency

Fig. 4 Computational scheme flow chart. The blocks highlighted in green are the ones developed specifically in this work.

III. Results

All CFD simulations of the cases presented have been performed by solving the compressible Euler equations using Roe's approximate Riemann solver with a limited second order MUSCL using Venkatakrishnan's slope limiter. The solution is brought to steady state through an implicit Euler scheme, all using the tools available in SU2 [15].

A. Validation

Table 1 Experimental setup data - NACA 23012 Papadakis et. al. [14]

Airfoil	NACA 23012
	$chord = 0.914\ m$
	$AoA = 2.5\ \text{deg}$
Airflow	EULER (in SU2 [15])
	$M_\infty = 0.22937$
	$P_\infty = 94802.914\ Pa$
	$T_\infty = 288.705\ K$
Cloud & Droplets	$LWC = 0.5\ g/m^3$
	$MVD = 20,\ 154\ \mu m$
	$\mu_P = 0.0011208\ Pa/s$
	$\rho_P = 1000\ kg/m^3$
	$\sigma_P = 0.074\ N/m$

The Eulerian droplet tracker has been validated here since it was purpose developed for this work. For this, the 2D NACA 23012 case from Papadakis et al. [14] has been used, with the experimental setup data reported in Table 1.

7

Results for *MVD* = 20 *µm* and *MVD* = 154 *µm* are reported in Fig. 4, with and without using MUSCL, in order to validate the spatial convergence of the Eulerian solver. It can be seen that using MUSCL results in a significantly faster mesh convergence: the collection efficiency computed over a mesh with 6000 *control volumes* agrees perfectly with the one computed over a reference mesh with 191000 *control volumes*, as shown in Fig. 5b. On the other hand, as displayed in Fig. 5a, not using MUSCL in the lower *MVD* = 20 *µm* case does not return mesh converged results with the 6000 *control volumes*. Conversely, in the SLD case, i.e., *MVD* = 154 *µm*, in Figs. 4c and 4d, all meshes and numerical settings yield almost identical results due to the ballistic nature of the droplets.

(a) MVD = 20μm (no MUSCL)

(b) MVD = 20μm (MUSCL)

(c) MVD = 154μm (no MUSCL)

(d) MVD = 154μm (MUSCL)
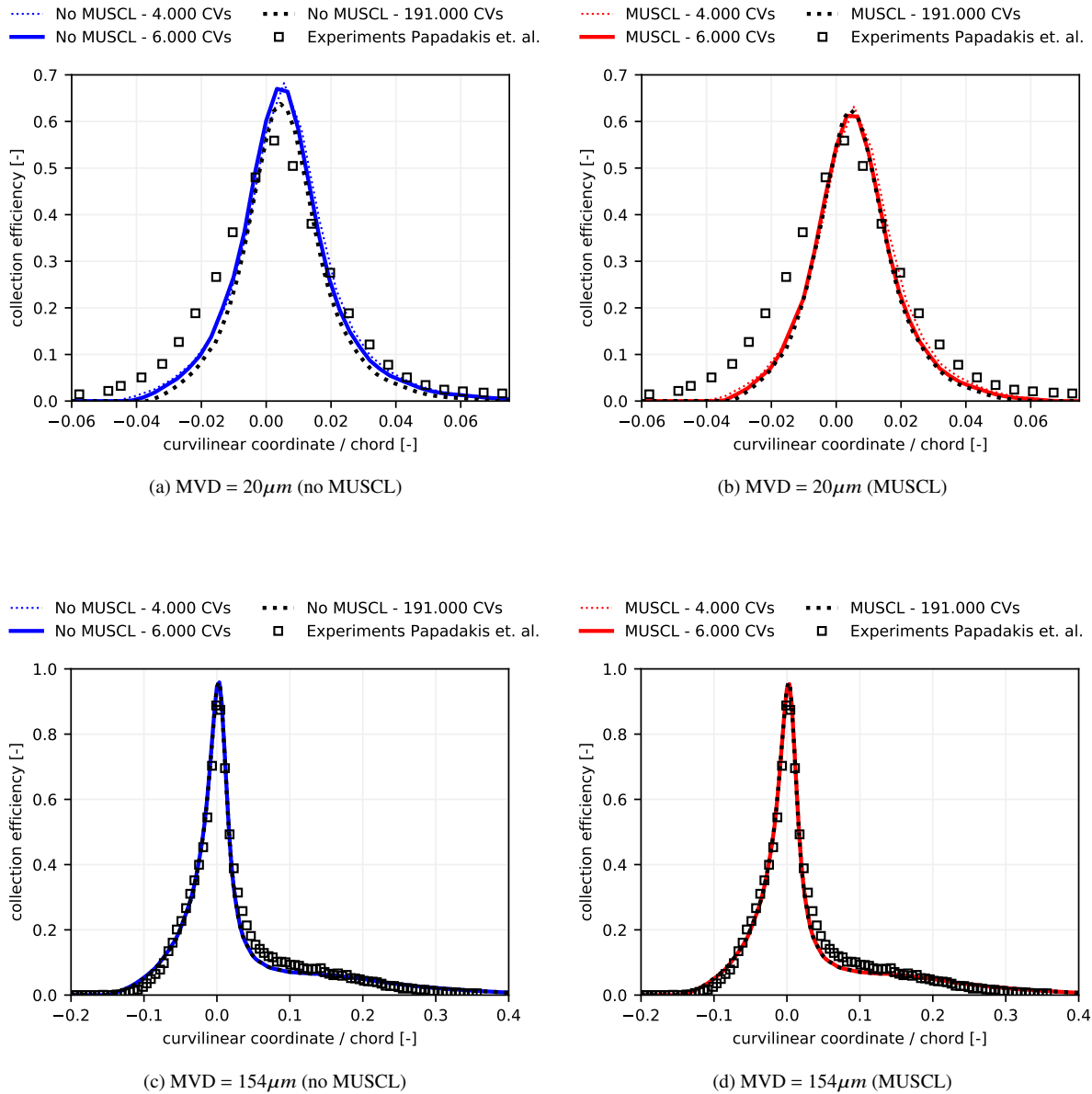
Fig. 4 Eulerian droplet tracking mesh convergence with and without MUSCL for NACA 23012, for two clouds with different MVDs. Experimental data are given by Papadakis et al. [14].

Comparing the results obtained on the 6000 *control volumes* mesh to the ones obtained with the Lagrangian droplet tracker PoliDrop on the same mesh and air-flow, for both 1 bin and 10 bins with *MVD* = 20μm there is good agreement regarding peak height and impingement limits with a slight deviation on the slopes (Fig. 5a). In the SLD case *MVD* = 154 *µm* (Fig. 5b) the differences are negligible due, again, to the ballistic nature of the droplets.

(a) MVD = $20\mu m$ (b) MVD = $154\mu m$
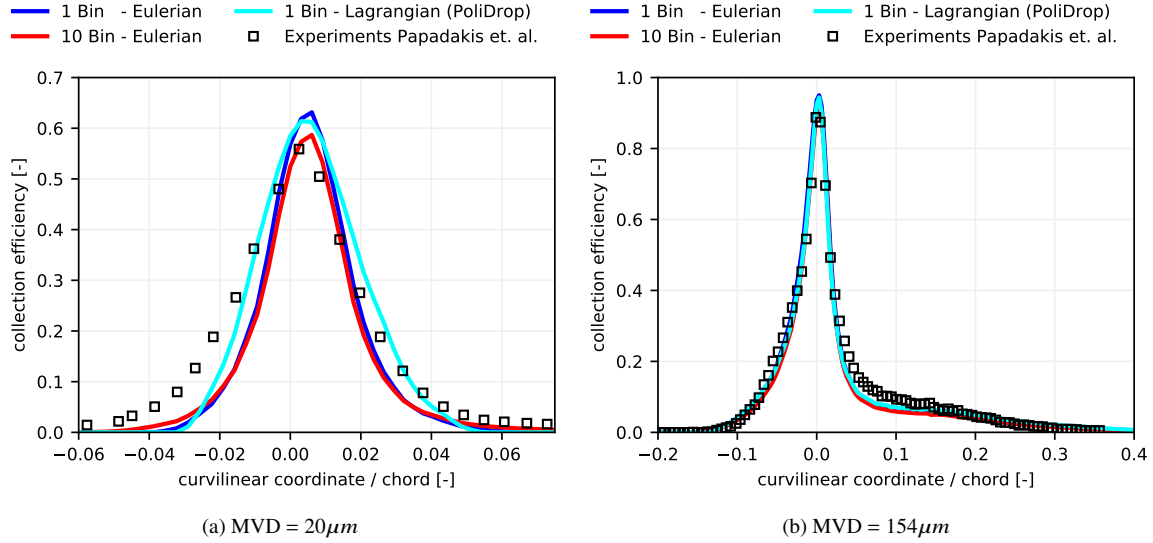
Fig. 5 **Eulerian droplet tracking for NACA 23012, considering 1 bin and 10 bins, compared to the Lagrangian tracking. Experimental data are given by Papadakis et al. [14].**

PoliDrop [19] has been used and tested thoroughly, therefore only the Lagrangian re-injection step is validated in this work. To do so, the secondary droplets have been re-injected directly into the NACA 23012 airfoil in order to check for mass conservation. This simple test consists in the following:

1) Compute the Eulerian free-stream droplet field solution (as normal)

    Correct the collection efficiency using the chosen splashing and bouncing model

    Compute the diameter and number of splashing and bouncing droplets per unit time

2) Re-inject the secondary droplets, not in the direction computed by the model but rather directly into the airfoil, exactly in the point where they splashed, as depicted in Fig. 6a

    Compute the re-injection collection efficiency and compare it to the correction, Fig. 6b

This test checks that the collection efficiency (a measure of the mass of water) being removed by the splashing model is mass conservative with respect to the collection efficiency being computed by the Lagrangian re-injection. The results are reported in Fig. 6b where the collection efficiency removed due to droplets splashing and bouncing is compared to the collection efficiency added by re-injecting directly into the airfoil, normal to the surface. A measure of the total mass of water, computed as the integral of the collection efficiency over the surface, $I = \int \beta(s)\mathrm{d}s$, is (approximately) conserved, and the small discrepancies in the shape of the two curves is due to the slight deviation of the droplet trajectories caused by the airflow.

B. Lagrangian Re-Injection

To test the effectiveness of the Lagrangian re-injection and its actual contribution in in-flight icing cases, two main cases have been chosen: a 2D multi-element airfoil and a 3D swept tail in a wind tunnel, both taken from the work of Papadakis et al. [6] and both in the SLD regime. The 2D NACA 23012 case presented in the validation section III.A has not been used in this section since, in a 2D setting with a single *non-concave* surface, all droplets that detach from the wall are carried away in the wake by the airflow with no significant downstream re-impingement. Re-impingement has an important impact on the collection efficiency when there are multiple stagnation points (such as over a multi-element airfoil) or when the flow presents strong three-dimensionality.

(a) Direct Re-Injection Sketch
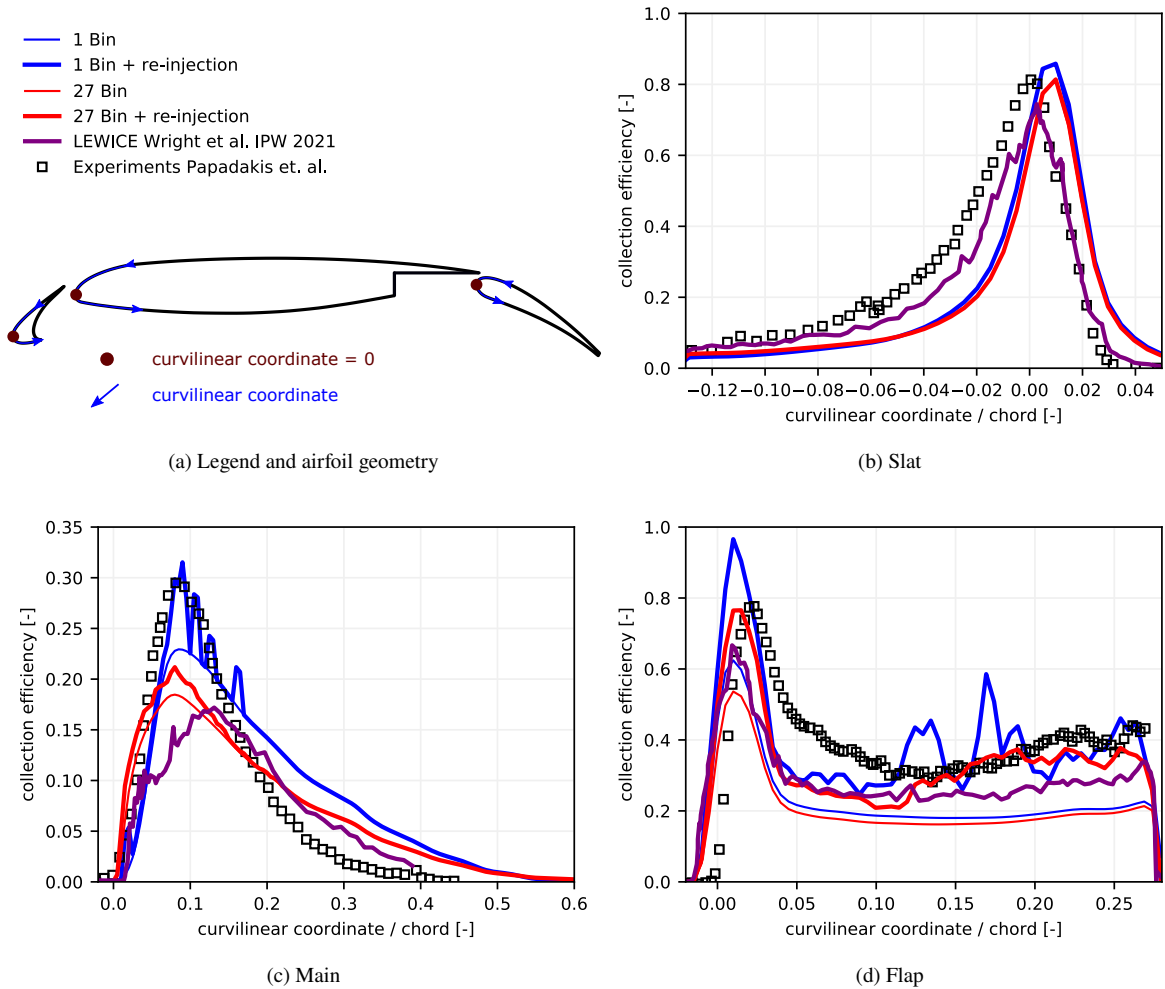
(b) Collection Efficiency Results
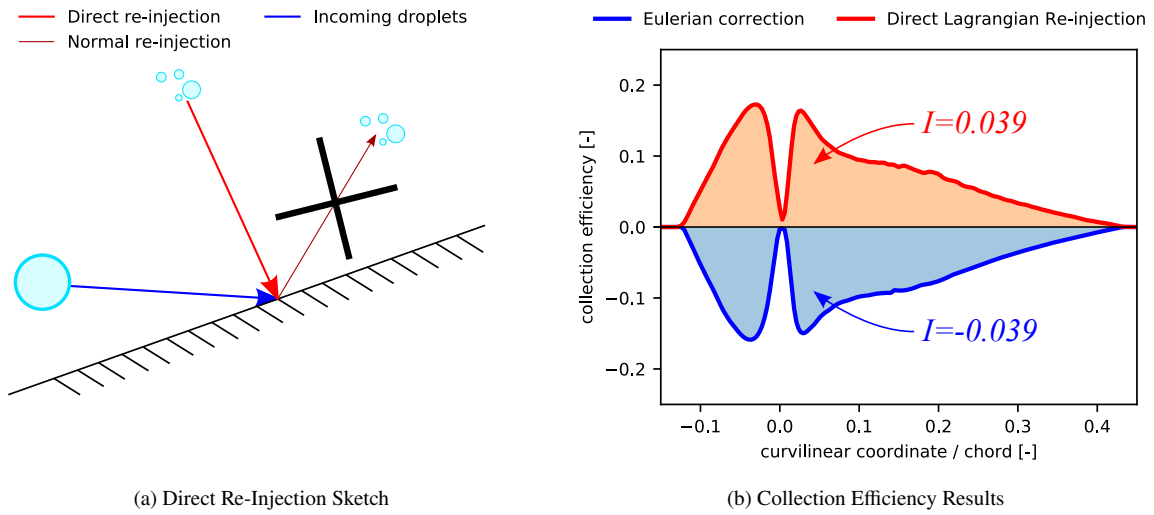
Fig. 6   Re-injection mass conservation test. Secondary droplets are re-injected directly onto the airfoil at the location where they splashed (as shown in 6a) and the collection efficiency is compared to the splashing correction applied to the free-stream collection efficiency to check mass conservation in 6b. A measure of the total mass of water $I = \int \beta(s)\mathrm{d}s$ proves mass conservation

1. Three-Element Airfoil 2D

Table 2   Experimental setup data three-element airfoil [6]

|	
Airfoil	Three Element Airfoil
	$chord = 0.914\ m$
	$AoA = 4\deg$
Airflow	EULER (in SU2 [15])
	$M_\infty = 0.233628$
	$P_\infty = 95630\ Pa$
	$T_\infty = 278\ K$
Cloud & Droplets	$LWC = 0.5\ g/m^3$
	$MVD = 92\ \mu m$
	$\mu_P = 0.0011208\ Pa/s$
	$\rho_P = 1000\ kg/m^3$
	$\sigma_P = 0.074\ N/m$

The first case presented is the three-element airfoil found in Papadakis et al. [6] with the experimental setup data reported in Table 2. Collection efficiency results are presented in Fig. 7 for a 1 bin and a 27 bin simulation, with and without Lagrangian re-injection. These results are also compared to experimental data from [6] and the numerical results presented at the 1st AIAA Ice Prediction Workshop (IPW) by Wright et al. [20] obtained using LEWICE with 27 bins.

(a) Legend and airfoil geometry

(b) Slat

(c) Main

(d) Flap

Fig. 7   Collection efficiency for MVD= 92μm using 1 and 27 bins for three element airfoil. Numerical results obtained with the proposed approach, with and without re-injection, are compared to numerical data by Wright et al. [20] and experimental data by Papadakis et al. [6]

The collection efficiency on the slat (Fig. 7b) appears to have an offset, most probably due to the difficulty in defining the *curvilinear coordinate* = 0 point. In this work, it is always defined as the point with min(x) in the geometry reference frame. As expected, there is virtually no re-injection contribution ($\sim$ 1.5% in Fig. 8a) due to the fact that this is the first surface droplets encounter. Looking at the main surface (Fig. 7c), the re-injection starts to contribute in a more significant manner to the collection efficiency, as Fig. 8b shows clearly with a 10% to 20% increase on the peak. The agreement with experimental data on the flap (Fig. 7d) increases significantly, with the peak almost matching perfectly for the 27 bin simulation. There is a significant improvement also on the rest of the flap's solution, with a collection efficiency increase ranging from $\sim$ 10% up to $\sim$ 40%, as can be seen in Fig. 8c.

Running a multi-bin simulation has proven crucial to obtaining a good re-injection correction, due to the more heterogeneous nature of the secondary droplets generated by the a multi-bin simulation. For each bin, a set of droplets is generated for each surface mesh element, this means that for a 27 bin simulation there are 27 different kinds of droplets being re-injected at the same location, with different diameter, speed and direction. In a single bin simulation, the droplets being re-injected are much more homogeneous, and this causes the formation of *trains* of almost identical droplets (appreciable in Fig. 9a) which in turn cause the peaks seen in Figs. 7c and 7d.
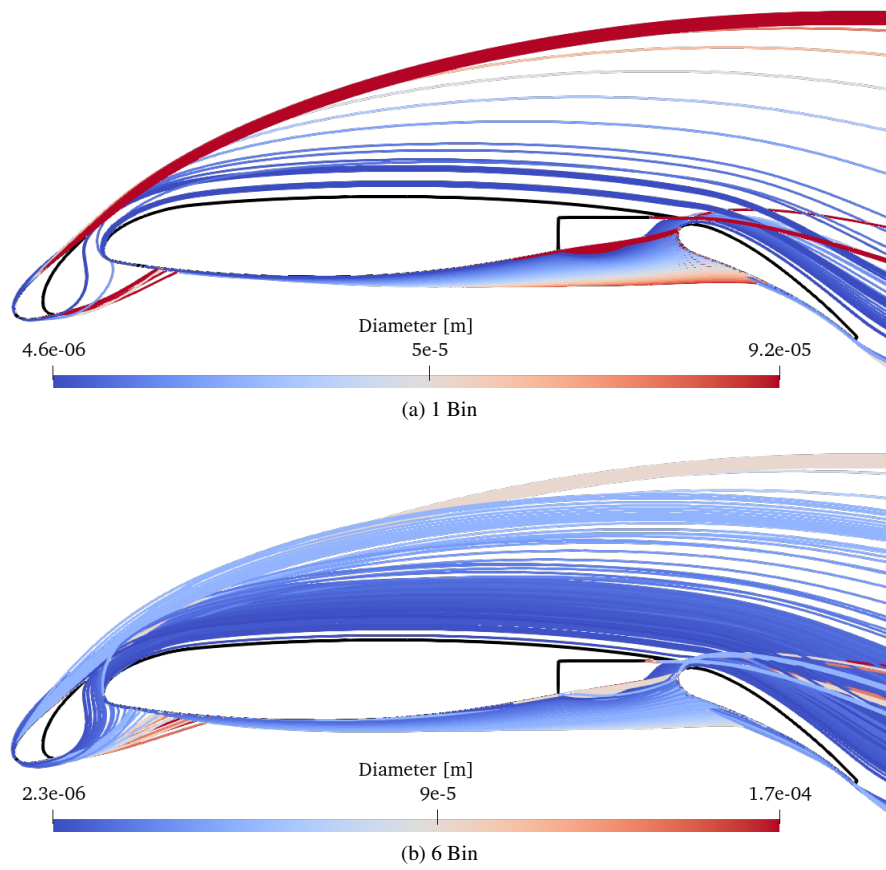
11
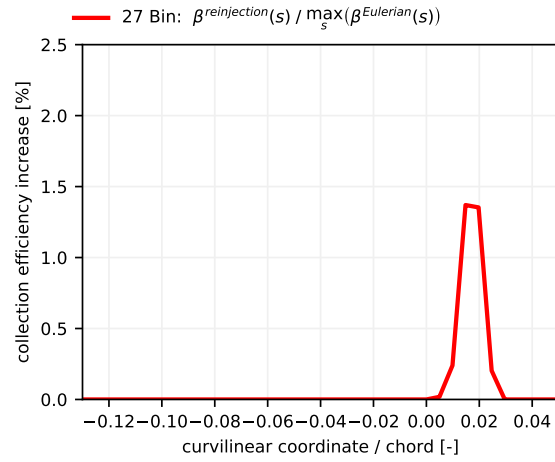
(a) Slat
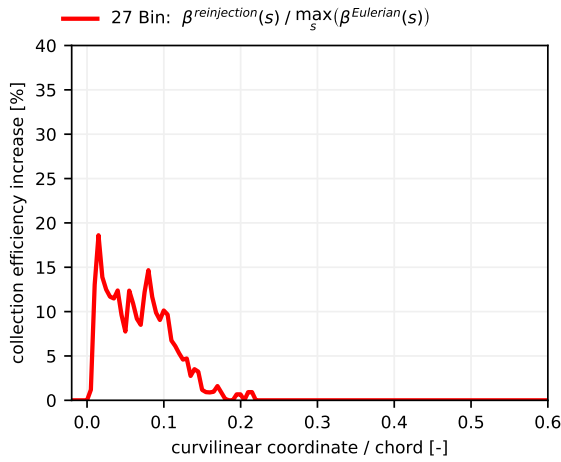
(b) Main
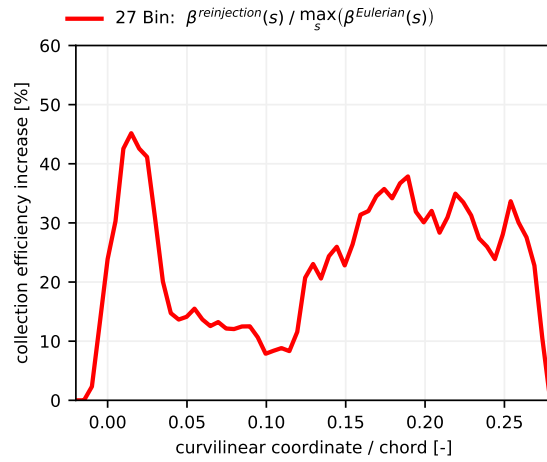
(c) Flap

Fig. 8 Collection efficiency percentage increase due to re-injection for MVD= 92μm using 27 bins for three element airfoil [6]

Diameter [m]

4.6e-06   5e-5   9.2e-05

(a) 1 Bin

Diameter [m]

2.3e-06   9e-5   1.7e-04

(b) 6 Bin

Fig. 9   Re-injected droplet trajectories for MVD= 92μm for three element airfoil [6]

Table 3   Experimental setup data HTail in wind tunnel [6]

Airfoil	NACA 64A008
	Mean Aerodynamic Chord = 0.95631 *m*
	AoA = 6 deg
Airflow	EULER (in SU2 [15])
	$M_\infty = 0.23$
	$P_\infty = 83025\ Pa$
	$T_\infty = 280\ K$
Cloud & Droplets	$LWC = 0.5\ g/m^3$
	$MVD = 92\ \mu m$
	$\mu_P = 0.0011208\ Pa/s$
	$\rho_P = 1000\ kg/m^3$
	$\sigma_P = 0.074\ N/m$

Another case of interest for the re-injection is the one of an horizontal tail empennage in a wind tunnel from [6] with the experimental setup data reported in Table 3. This case has been chosen due to the intrinsic three-dimensionality and the availability of experimental measurements of the collection efficiency. Firstly, the pressure coefficient measured at a distance $z = 0.914\ m$ from the wind tunnel floor is compared to the experimental data from Papadakis et al. [6] to assess the quality of the solution in Fig. 10.
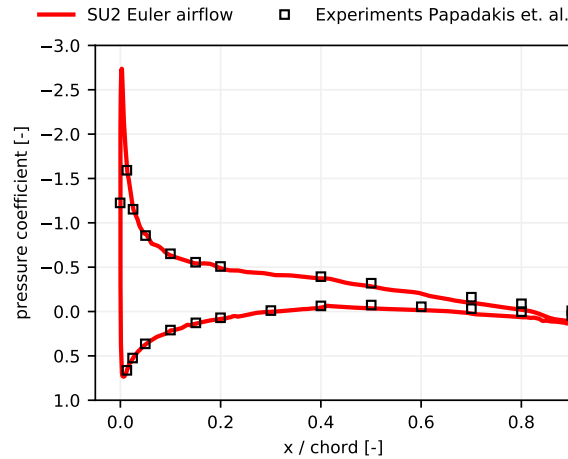

Fig. 10   Pressure coefficient at z = 0.914m from wind tunnel floor for 3D horizontal tail. Numerical results are compared to experimental data by Papadakis et al. [6] to assess airflow solution quality

The collection efficiency for a 1 bin and a 27 bin simulation are displayed in Fig. 11. As discussed before, when using a single bin the correction becomes very *monochromatic* due to the homogeneousness of the re-injected droplets. As seen in Fig 9a, when using a single bin, re-injected droplets tend to create individual *trains* of droplets, since most of them are of similar size and are re-injected roughly in the same area, therefore they tend to re-impinge in a similar location. This makes the correction for the 1 bin simulation (Fig. 11a) very localized in one spot. This is particularly visible when compared to the 27 bin simulation (Fig. 11b). Three-dimensionality does indeed cause some re-impingement of secondary droplets (with a local maximum of up to 5% in the 27 bin simulation) but not to the extent found when considering complex geometries with multiple consecutive stagnation points.
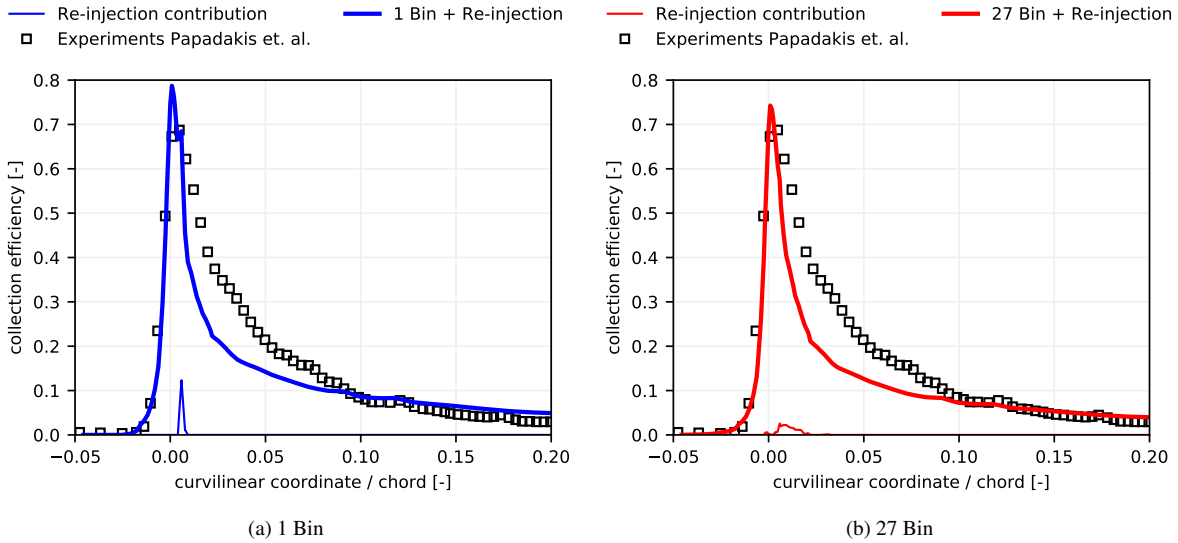
Fig. 11 **Collection efficiency at z = 0.914 m from wind tunnel floor with MVD= 92μm for 3D horizontal tail. Numerical results obtained with the proposed approach, using 1 and 27 bins, are compared to experimental data by Papadakis et al.[6]. For each test, the contribution due to re-injection is also displayed standalone.**

The results of the proposed approach compare favourably with LEWICE and GlennICE simulation data presented at 1st AIAA IPW by Wright et al. [20], as shown in Fig. 12, where we can observe a fair agreement on the peak and impingement limits, especially with the LEWICE data, whereas GlennICE data show a strong over-prediction far from the peak. The 3D collection efficiency map is shown in Fig. 13.
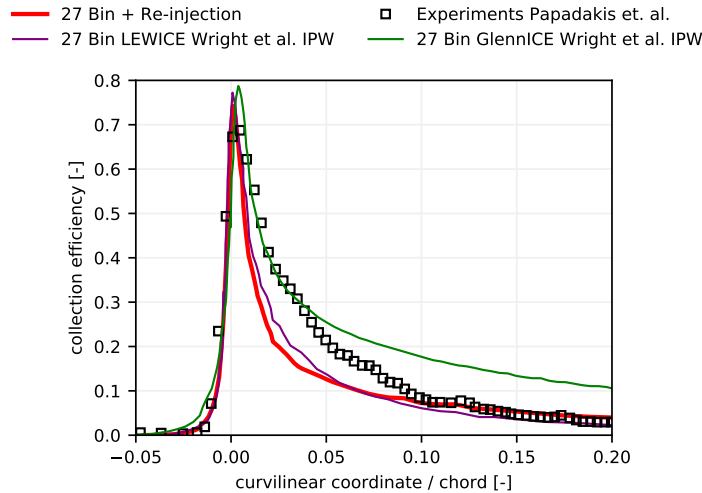
Fig. 12 **Collection efficiency at z = 0.914m from wind tunnel floor with MVD= 92μm for 3D horizontal tail. Numerical results obtained with the proposed approach are compared to numerical data presented at AIAA 1st IPW [20] and experimental data [6].**

For this test, computational times have been measured in order to quantify the computational cost of the Lagrangian re-injection step and verify that the bin restart procedure implemented for Eulerian multi-bin simulations is indeed decreasing the computational cost. In Fig. 14a, the computational times are plotted as function of the number of bins, with and without bin restart. The computational cost of the Eulerian simulations remains linear when using the bin

15
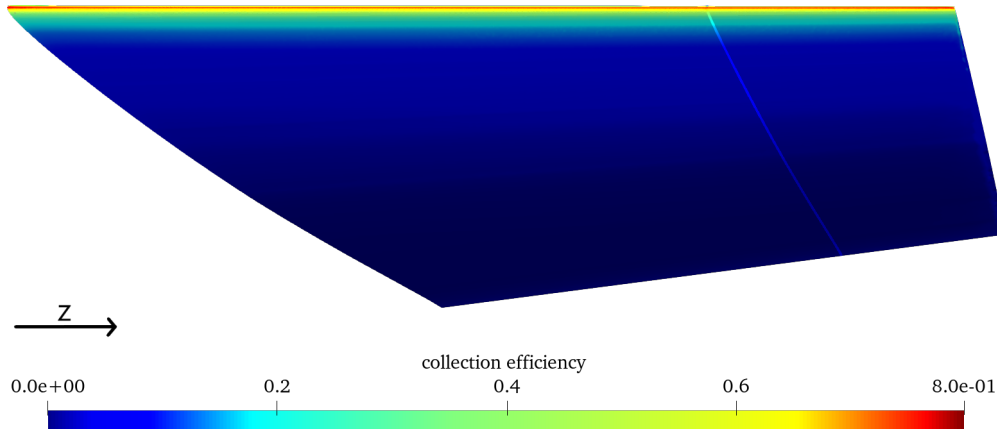
Fig. 13 Collection efficiency map for MVD= 92μm using 27 bins for 3D horizontal tail

restart, but with a significant decrease in the slope (about -65%). This is even more evident when looking at Fig. 15 where the root-mean-square (RMS) of the residuals across iterations shows that a 27 bin simulation with bin restart takes less iterations to reach convergence than a 6 bin simulation without bin restart. This means that the bin restart procedure allows us to reach a higher quality solution (that is using 27 bins rather than 6 bins) while taking a similar number of iterations.

The Lagrangian re-injection step increases the computational cost by roughly 30% over the bin restart Eulerian simulations. This percentage increase remains somewhat constant due to the fact that the Lagrangian droplet tracking cost increases with the number of bins linearly too, due to the linear increase of re-injected droplets (Fig. 14b).

(a) Computational Time

(b) Number of Re-injected Droplets
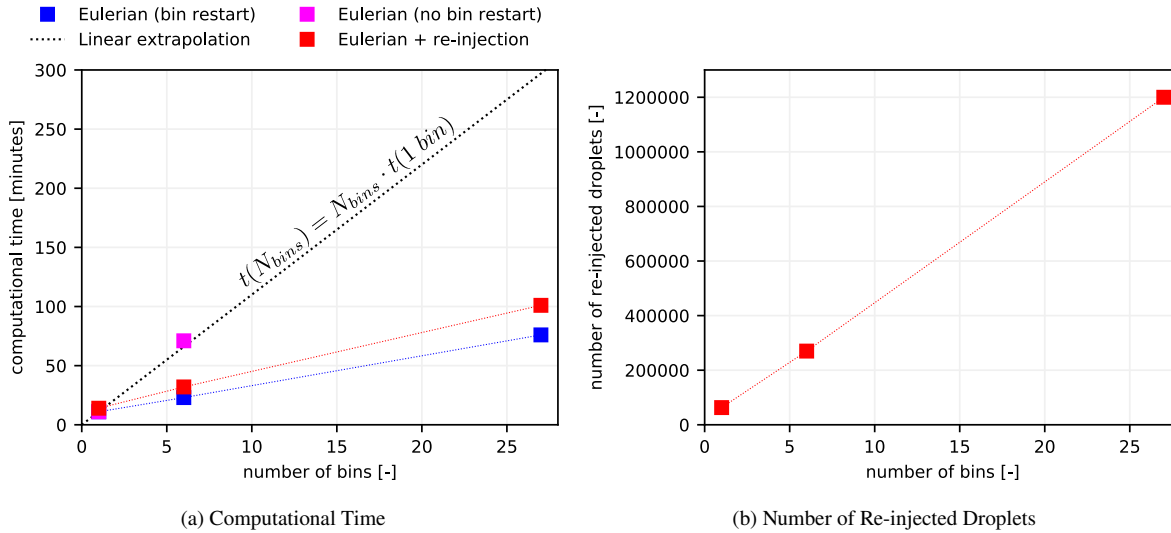
Fig. 14 Computational time 14a with and without bin restart on 6 cores @2.5GHz and number of re-injected droplets 14b for 3D horizontal tail

16
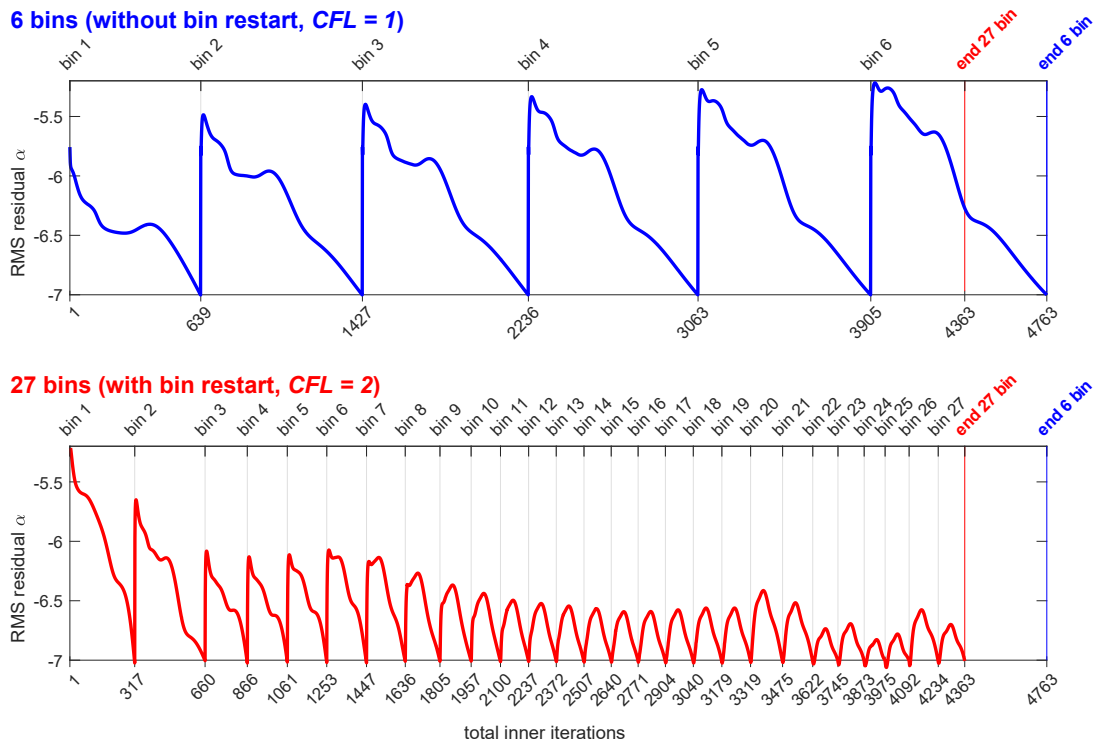
Fig. 15 RMS residual of the volume fraction α with and without bin restart for the 3D horizontal tail. A 6 bin simulation without bin restart takes more iterations than a 27 bin simulation with bin restart, with the 27 bin simulation also yielding a much higher quality collection efficiency prediction.

IV. Conclusion

The tools developed in this work allow for a better prediction of the collection efficiency in three-dimensional or complex multi-element cases for in-flight icing applications in Appendix O conditions by considering a comprehensive set of the physical phenomena occurring (poly-disperded droplets impinging, splashing, bouncing and re-impinging) while also mitigating, where possible, the inherent computational costs of simulating them. An Eulerian multi-bin droplet tracker with a Lagrangian re-injection step for secondary droplets has been developed. The Lagrangian re-injection step has been found to increase the experimental agreement of the collection efficiency prediction significantly for aft surfaces in multi-element airfoils. Also, flow three-dimensionality contributes (to a smaller degree) to the re-impingement physics, even in single element geometries. The computational cost of re-injecting droplets has been decreased significantly by using a Lagrangian approach, rather than remaining in the Eulerian framework. Also, the computational cost of a multi-bin Eulerian simulation has been decreased by simply using the converged solution for the previous bin as the initial guess for the following bin, instead of the classical homogeneous guess.

Further work would attempt to include the poly-dispersed Eulerian-Lagrangian particle tracking strategy, here proposed, in the whole process of in-flight ice accretion simulation, within the PoliMIce software suite [21] to investigate the effects of re-impingement on ice shapes, as well as its evolution in unsteady simulations. In these ones, to compute the correct impingement location, the body-fitted mesh must be re-generated to comply with the new ice shape. This task may be accomplished by using conservative mesh adaptation techniques [22, 23] or ad hoc immersed boundary layer methods [24]. In addition, the gain in the computation cost of the proposed strategy could pave the way for further improvements on the modeling side. In particular, particle breakup models [12] could be added to the Lagrangian re-injection step, with a close eye on the computational cost generated by the shear amount of droplets that would be created.

Acknowledgments

References

[1] Papadakis, M., Yeong, H. W., and Suares, I. G., "Simulation of ice shedding from a business jet aircraft," *45th AIAA Aerospace Sciences Meeting*, Vol. 9, 2007, pp. 6093–6117. https://doi.org/10.2514/6.2007-506, AIAA 2007-506.

[2] Saurel, R., and Abgrall, R., "A Multiphase Godunov Method for Compressible Multifluid and Multiphase Flows," *J. Comput. Phys.*, Vol. 150, No. 2, 1999, pp. 425–467. https://doi.org/10.1006/JCPH.1999.6187.

[3] Re, B., and Abgrall, R., "Non-equilibrium Model for Weakly Compressible Multi-component Flows: The Hyperbolic Operator," *Lecture Notes in Mechanical Engineering*, 2020, pp. 33–45. https://doi.org/10.1007/978-3-030-49626-5_3.

[4] Kapila, A. K., Menikoff, R., Bdzil, J. B., Son, S. F., and Stewart, D. S., "Two-phase modeling of deflagration-to-detonation transition in granular materials: Reduced equations," *Phys. Fluids*, Vol. 13, No. 10, 2001, pp. 3002–3024. https://doi.org/10.1063/1.1398042.

[5] Bourgault, Y., Habashi, W. G., Dompierre, J., and Baruzzi, G. S., "A finite element method study of Eulerian droplets impingement models," *International Journal for Numerical Methods in Fluids*, Vol. 29, No. 4, 1999, pp. 429–449. https://doi.org/https://doi.org/10.1002/(SICI)1097-0363(19990228)29:4<429::AID-FLD795>3.0.CO;2-F.

[6] Papadakis, M., Hung, K. E., Vu, G., Yeong, H.-W., Bidwell, C. S., Breer, M. D., and Bencic, T. J., "Experimental Investigation of Water Droplet Impingement on Airfoils, Finite Wings, and an S-duct Engine Inlet," Tech. Rep. 2002-211700, NASA, October 2002.

[7] Cao, Y., and Xin, M., "Numerical Simulation of Supercooled Large Droplet Icing Phenomenon: A Review," *Archives of Computational Methods in Engineering*, Vol. 27, 2020, pp. 1231–1265. https://doi.org/10.1007/s11831-019-09349-5, URL https://doi.org/10.1007/s11831-019-09349-5.

[8] Bilodeau, D., Habashi, W., Fossati, M., and Baruzzi, G., "Eulerian Modeling of Supercooled Large Droplet Splashing and Bouncing," *Journal of Aircraft*, Vol. 52, 2015, pp. 1611–1624. https://doi.org/10.2514/1.C033023.

[9] Berthon, C., Breuß, M., and Titeux, M.-O., "A relaxation scheme for the approximation of the pressureless Euler equations," *Numerical Methods for Partial Differential Equations*, Vol. 22, No. 2, 2006, pp. 484–505. https://doi.org/https://doi.org/10.1002/num.20108.

[10] Wright, W., "Further Refinement of the LEWICE SLD Model," *44th AIAA Aerospace Sciences Meeting and Exhibit*, 2006. https://doi.org/10.2514/6.2006-464, AIAA 2006-464.

[11] Rutkowski, A., Wright, W., and Potapczuk, M., "Numerical Study of Droplet Splashing and Re-impingement," *41st Aerospace Sciences Meeting and Exhibit*, 2003. https://doi.org/10.2514/6.2003-388, AIAA 2003-388.

[12] Tan, C., and Papadakis, M., "Droplet Breakup, Splashing and Re-Impingement on an Iced Airfoil," *4th AIAA Theoretical Fluid Mechanics Meeting*, 2005. https://doi.org/10.2514/6.2005-5185, AIAA 2005-5185.

[13] Fouladi, H., Baruzzi, G. S., Nilamdeen, S., and Ozcer, I., "Numerical Modelling of Primary and Secondary Effects of SLD Impingement," *International Conference on Icing of Aircraft, Engines, and Structures*, SAE International, 2019, pp. 1–11. https://doi.org/https://doi.org/10.4271/2019-01-2002.

[14] Papadakis, M., Rachman, A., Wong, S.-C., Yeong, H.-W., Hung, K. E., and Bidwell, C. S., "Water Impingement Experiments on a NACA 23012 Airfoil with Simulated Glaze Ice Shapes," *42nd AIAA Aerospace Sciences Meeting and Exhibit*, 2004. https://doi.org/10.2514/6.2004-565, AIAA 2004-565.

[15] Palacios, F., Colonno, M., Aranake, A., Campos, A., Copeland, S., Economon, T., Lonkar, A., Lukaczyk, T., Taylor, T., and Alonso, J., "Stanford University Unstructured (SU2): An open-source integrated computational environment for multi-physics simulation and design," *51st AIAA Aerospace Sciences Meeting including the New Horizons Forum and Aerospace Exposition*, 2013. https://doi.org/10.2514/6.2013-287, AIAA 2013-287.

[16] Morrison, F. A., *An Introduction to Fluid Mechanics*, Cambridge University Press, 2013.

[17] Clift, R., Grace, J., and Weber, M., *Bubbles, drops, and particles*, Academic Press, New York, 1978.

[18] Honsek, R., and Habashi, W., "FENSAP-ICE: Eulerian Modeling of Droplet Impingement in the SLD Regime of Aircraft Icing," *44th AIAA Aerospace Sciences Meeting and Exhibit*, 2006. https://doi.org/10.2514/6.2006-465, AIAA 2006-465.

[19] Bellosta, T., Parma, G., and Guardone, A., "A Robust 3D Particle Tracking Solver for in-Flight Ice Accretion Using Arbitrary Precision Arithmetic," *Proceedings of the VIII International Conference on Computational Methods for Coupled Problems inScience and Engineering*, edited by M. P. E. Onate and B. Schrefl, CIMNE, 2019, pp. 41,50.

[20] Wright, W., Rigby, D., Galloway, E., and Potapczuk, M., "LEWICE and GlennICE Results for Ice Prediction Workshop," URL: https://icepredictionworkshop.wordpress.com/results/, 8 2021.

[21] Gori, G., Zocca, M., Garabelli, M., Guardone, A., and Quaranta, G., "PoliMIce: A simulation framework for three-dimensional ice accretion," *Appl. Math. Comput.*, Vol. 267, 2015, pp. 96–107. https://doi.org/10.1016/j.amc.2015.05.081.

[22] Cirrottola, L., Ricchiuto, M., Froehly, A., Re, B., Guardone, A., and Quaranta, G., "Adaptive deformation of 3D unstructured meshes with curved body fitted boundaries with application to unsteady compressible flows," *J. Comput. Phys.*, Vol. 433, 2021, p. 110177. https://doi.org/https://doi.org/10.1016/j.jcp.2021.110177.

[23] Colombo, S., and Re, B., "An ALE residual distribution scheme for the unsteady Euler equations over triangular grids with local mesh adaptation," *Computers & Fluids*, Vol. 239, 2022, p. 105414. https://doi.org/https://doi.org/10.1016/j.compfluid.2022.105414.

[24] Donizetti, A., Re, B., and Guardone, A., "A level-set based mesh adaptation technique for mass conservative ice accretion in unsteady simulations," *9th edition of the International Conference on Computational Methods for Coupled Problems in Science and Engineering*, edited by E. Oñate, M. Papadrakakis, and B. Schrefler, CIMNE, 2021, pp. 1–12. https://doi.org/10.23967/coupled.2021.004.